NASA Technical Memorandum 103969

Sol-Gel Synthesis and Densification of Aluminoborosilicate Powders Part 2–Densification

Jeffrey Bull, Guna Selvaduray, and Daniel Leiser

September 1992

NASA
National Aeronautics and Space Administration

NASA Technical Memorandum 103969

Sol-Gel Synthesis and Densification of Aluminoborosilicate Powders Part 2–Densification

Jeffrey Bull, Ames Research Center, Moffett Field, California
Guna Selvaduray, San Jose State University, San Jose, California
Daniel Leiser, Ames Research Center, Moffett Field, California

September 1992

National Aeronautics and
Space Administration

Ames Research Center
Moffett Field, California 94035-1000

SOL-GEL SYNTHESIS AND DENSIFICATION OF ALUMINOBOROSILICATE POWDERS PART II—DENSIFICATION

Jeffrey Bull, Guna Selvaduray,* and Daniel Leiser
NASA Ames Research Center

Summary

Aluminoborosilicate (ABS) powders, high in alumina content, were synthesized by the sol-gel process utilizing four different methods of synthesis. The effect of these methods on the densification behavior of ABS powder compacts was studied. Five regions of shrinkage in the temperature range 25–1184°C were identified. In these regions, the greatest shrinkage occurred between the gel-to-glass transition temperature (T_g ≈835°C) and the crystallization transformation temperature ($T_t \approx 900°C$). The dominant mechanism of densification in this range was found to be viscous sintering. ABS powders were amorphous to X-rays up to T_t at which a multiphasic structure crystallized. No $2Al_2O_3 \cdot B_2O_3$ was found in these powders as predicted in the phase diagram. Above T_t densification was the result of competing mechanisms including grain growth and boria fluxed viscous sintering. Apparent activation energies for densification in each region varied according to the method of synthesis.

Introduction

Aluminoborosilicate (ABS) powder, high in alumina, is an attractive choice for application in high-temperature materials. It may be used as a boria (B_2O_3) diffusion source in the fabrication of silica-base fibrous thermal insulation to promote silica fiber-to-fiber bonding. When used as such, it is desirable that the boria exists as a fugitive component, so that after processing an aluminosilicate remains, thereby enhancing the temperature resistance of the resultant system. Recent studies of gel-derived silicates have found that they densify via several different mechanisms. Brinker and Mukerjee (ref. 1) showed that there were at least three densification mechanisms operative during the gel-to-glass transition of monolithic multicomponent gels: volume relaxation, condensation reactions, and viscous sintering. It has been suggested (refs. 2 and 3) that molecular-structural variations induced during the sol-gel synthesis of an inorganic polymer can influence its thermochemical and thermomechanical properties and hence its high-temperature behavior, e.g., structure, viscosity, and sinterability. Hence, the sol-gel synthesis of aluminoborosilicate powder may provide a material with the requisite properties. Therefore a study was initiated to synthesize aluminoborosilicate (ABS) powders utilizing several variations of the sol-gel process and to ascertain the effect of those methods on powder properties and densification behavior.

Several methods of synthesizing ABS powders, with the target composition of 62 wt% Al_2O_3/ 14 wt% B_2O_3/ 24 % SiO_2, via the sol-gel process have recently been reported (ref. 4). It was found that the method of synthesis affected particle size, morphology, and compaction trends. Thermochemically, the powders were quite similar with nearly equal weight loss histories and exhibiting a T_g of approximately 835°C. An exothermic reaction occurred at approximately 900°C for all powders and was attributed to a crystalline transformation. The powders were amorphous by powder X-ray diffraction (XRD) below this temperature. This study focuses on the effect that these methods of synthesis had on the thermal densification behavior.

Experimental

Details of ABS powder syntheses and subsequent compaction are presented in an earlier paper (ref. 4). Two synthesis methods were used, each utilizing two different alumina precursors. These were designated

*San Jose State University, San Jose, California.

I.ABS.1 for Method I using aluminum isopropoxide (AIP), I.ABS.2 with aluminum secbutoxide (ASB), and II.ABS.1 and II.ABS.2 for Method II using AIP and ASB, respectively.

A flow diagram depicting the post synthesis processing of the powders is shown in figure 1. After drying, the powders were ground with a porcelain mortar and pestle and then precalcined at 600°C for 2 h in flowing air. Elemental analysis of the powders at this stage of processing showed that the composition totaled $\approx$ 87 wt% metal oxides. The precalcined powder was sieved through an 80-mesh sieve and any agglomerates not able to freely pass through the screen were ground again. Two passes were all that were required. Powder compacts were formed by dry pressing in a carbon steel die which was sprayed with zinc stearate for lubrication. Powder compact weights and dimensions were measured and bulk densities calculated. Apparent density was calculated from the previously recorded weight and apparent volume obtained from helium pycnometry. The powder compacts were then individually placed in a horizontal dilatometer for thermal dilatometric analysis (TDA). Both isothermal and constant heating rate (CHR) experiments were conducted on the powder compacts in air. Corrections for thermal expansion due to system (alumina) and sample expansion were applied to the raw data during conversion to engineering units. A value of 3.8 X 10^{-6}/°C over the temperature range 25°C–700°C was experimentally determined to be the linear coefficient of thermal expansion (LCTE) for the ABS powder compacts. Immediately after each run, bulk and apparent densities were measured before additional characterization.

After heat treatment, representative powder compacts were ground to a fine powder and 100 mg of this powder were dissolved in a dilute HF/HNO_3 solution for elemental analysis using inductively coupled plasma atomic emission spectroscopy (ICP-AES). The remaining powder from each sample was used for infrared spectroscopy (IR) utilizing the potassium bromide (KBr) disc method and also for XRD employing a $Cu_{K\alpha}$ radiation source. Vickers microhardness testing was done on a representative powder compact using a diamond indenter and an applied load of 1 kg. Scanning electron microscopy (SEM) was used to examine the morphology of powder compact fracture surfaces.

Results

Dilatometry

Linear shrinkage ($\Delta L/L_o$) in the ABS powder compacts was characterized by five major regions of shrinkage (fig. 2) when subjected to CHR (5°C/min.) conditions. These regions were designated A–E for low to high temperatures. Region A covers room temperature to 100°C, region B from 100–400°C, region C from 400–800°C, region D from 800 to about 900°C, and finally region E from about 900–1184°C.

Several temperatures in regions B–E were selected for isothermal TDA. Representative linear shrinkage vs. time and the corresponding log-log plots for regions B–E are shown in figures 3–6, respectively. The time dependence of linear shrinkage can usually be described in the form of a parabolic rate law expressed as

$$\frac{\Delta L}{L_o} = Kt^n \qquad (1)$$

where K is a material constant, t is time, and n is the coefficient of shrinkage (refs. 5 and 6). Hence, n can be found from the slope of a $\log(\Delta L/L_o)$ vs. $\log t$ plot. These values and their applicable regions are given in table 1. It was determined that all ABS powder compacts densified by viscous flow in region D since the initial values of n for short times ($t \leq 10$ min) in this region was ≈ 1. Accordingly then, the Frenkel model is applicable for this region (ref. 7). Linear shrinkage plots of this region are characterized by an initial high rate of shrinkage, gradually tapering off according to the sintering temperature and method of synthesis. As the curves in these figures suggest, n gradually decreased, in some cases to almost zero with increasing time. Figure 7 shows the variation in shrinkage of the ABS powder compacts for temperatures within regions C–E. The powder compacts in this figure show the densification behavior presented thus far.

Compositional and Structural Evolution

Weight loss occurred during the densification of ABS powder compacts although there was no significant difference in the weight loss between powder compacts prepared by different methods. Figure 8 shows the mean recorded weight loss of the powder compacts in the temperature interval studied along with the

mean fractional shrinkage for comparison. The resulting weight loss curve (fig. 8) roughly parallels those obtained from TGA (fig. 2, ref. 4).

Figure 9 shows XRD diffractograms of an ABS powder after isothermal treatments. The powders were amorphous up to a temperature of $\approx$ 864°C whereupon an ordering in the structure is evident by the appearance of broad diffraction lines. The diffraction lines at 2θ values of approximately 38 and 45° in the low temperature patterns were attributed to the decomposition products of zinc stearate, the die lubricant. These peaks were not present in XRD patterns of the same powders run before compaction. Intensities of the diffraction lines increased with increasing temperature corresponding to the formation of a more coherent lattice. Figure 10(a) shows the XRD pattern and d-spacings of major diffraction lines in II.ABS.2 after 1 h at 1400°C. This XRD pattern is typical of all ABS powders and indicates that no significant structural change occurred from 1184°C to 1400°C with the exception of additional grain growth.

Figure 10(b) shows the stick patterns of three candidate phases that were identifed in the ABS powders (ref. 8). Mullite and aluminum borate are equilibrium compounds as indicated in the phase diagram of figure 1 (ref. 4). Many of the diffraction lines of the candidate phases have the same or nearly the same *d*-spacing. Line superposition and the fact that agreement is obtained for some *d* values but not for all the corresponding intensities permit only tentative identification of a multiphasic structure (ref. 9). The absence of some lines, e.g., $d_{h,k,l} = 2.21$ of mullite, and the lack of agreement in intensities suggests that this phase is metastable. Clearly, the ABS powders are multiphasic above 1000°C with a pseudo-mullite structure being the most abundant. It is noteworthy that no $2Al_2O_3 \cdot B_2O_3$ was detected in any of the powders as predicted in the phase diagram.

Crystallite size analysis was undertaken based on the Scherrer technique using the diffraction line at 26.402 degrees two theta and a value of 0.94 as the calibration constant. The values shown in table 2 were determined after 1 h at the indicated temperature. The crystallites have a breadth initially of the order of 10 nm — close to that reported as the ultimate particle size in alkoxide gels (ref. 10). Crystallite size increased with increasing temperature in all powders.

The IR spectra of I.ABS.1 and II.ABS.2 for various temperatures are shown in Figures 11(a) and (b), respectively. The characteristic absorptions and their assignments are shown in figure 11(a) (refs. 11-13). These figures illustrate the major differences found in the IR spectra of the synthesized powders. The intensity of the absorption band at "a" gradually diminished with increasing temperature and shifted to a lower frequency. The band at "b" decreased with increasing temperature. Neither of these bands appeared in the powders at 845°C. The weak absorption band at "a" is still present in the IR spectra at temperatures greater than 690°C, but it was also present in the IR spectrum of the blank KBr disc and therefore is not related to the structure of the ABS powder. At 864°C these bands reappear in ASB based material and once again are absent at higher temperatures.

The fractured surface of a green powder compact pressed from AIP based ABS powder is shown in figure 12(a) and (c). Figure 12(b) and (d) shows micrographs of an AIP based powder compact after exposure to 1184°C for 1 h. Likewise, green ASB based powder compacts are shown in figure 13(a) and (c) while figure 13(b) and (d) shows an ASB based powder compact after 1 h at 1184°C. The particulate nature of both AIP and ASB based powder compacts is clearly apparent from these micrographs. Particle growth and coalescence is also evident from comparison of the higher magnification micrographs before and after firing. Particle growth appears from the micrographs to be of similar magnitude in both AIP and ASB powders. The particles measure less than a micron after compaction and $\approx 1\mu$m after firing at 1184°C for 1 h.

Powder Compact Properties

Mean apparent density, bulk density, and microhardness measurements of the powder compacts were performed after selected heat treatments. Bulk density of the powder compacts initially decreased slightly with increasing temperature as shown in figure 14. Brinker *et al.* (ref. 14) have reported similar behavior but also observed a decrease in apparent density accompanying the decrease in bulk density. They attributed this to desorption of physically adsorbed water and solvent from the gel and to pyrolysis of unhydrolyzed alkoxy groups. No such decrease was observed in the apparent density of ABS powder compacts as the powders had already been subjected to heat treatment (2 h at

600°C) during which the apparent density increased by 28% (ref. 4). The powder compacts increased in bulk density by 80% and in apparent density by approximately 32%. Thus, powder compact densification was characterized by a large decrease in volume by skeletal shrinkage with a gradual elimination of porosity. According to the rule of mixtures 55% of theoretical density was obtained after 1 h at 1184°C.

Vickers microhardness testing was conducted on II.ABS.1 powder compacts fired at selected temperatures for 1 h within each major region of shrinkage. As shown in figure 15, the hardness increased with increasing temperature up to 864°C. Above this temperature the hardness value drops to that measured at 845°C. There was only a slight additional increase in hardness at higher temperatures. Firing the ABS powder compacts in the region of viscous flow resulted in the highest values of hardness.

Discussion

The intercept of $\log(\Delta L/L_o)$ vs. $\log t$ plots with the ordinate is the logarithm of the material constant K. This constant is dependent on temperature and the nature of the material. The activation energy required for densification may be calculated by assuming K obeys an Arrhenius relationship, that is

$$K = K_o exp(-Q/RT) \qquad (2)$$

where K_o is a constant, Q the activation energy, and T the absolute temperature. A $\log K$ vs. $1/T$ plot yields a straight line with $-0.43Q/R$ slope. However, to apply equation (2), the shrinkage coefficient n in equation (1) must be a constant. Within experimental error, this is the case for regions C and E and these plots provided straight lines from which Q was calculated. Densification in region D was attributed to viscous flow for which n in equation (1) equals one. The decreasing shrinkage rate that is observed in figure 5(a) prevented the application of equation (2). However, since sintering occurred by viscous flow, CHR experiments were applied using Frenkel's model in the following form:

$$\frac{\Delta L}{L_o} = \frac{\gamma}{2r\eta} t \qquad (3)$$

where γ is the surface energy, r the particle radius, and η the viscosity. Assuming that $\eta = Aexp(Q/RT)$ where A is the frequency factor and expressing the heating rate by $\nu = dT/dt$, equation (3) becomes

$$\frac{d}{dt}\left(\frac{\Delta L}{L_o}\right) = \left(\frac{\gamma}{2rA\nu}\right) exp(-Q/RT) \qquad (4)$$

If γ and A are independent of temperature, this equation can be integrated and becomes (refs. 5 and 15)

$$\frac{\Delta L}{L_o} = \left(\frac{\gamma RT^2}{2rA\nu Q}\right) exp(-Q/RT) \qquad (5)$$

A plot of $\log(\Delta L/L_o \cdot 1/T^2)$ vs. $1/T$ for region D was linear and gave a slope of $-0.43Q/R$ from which Q was calculated. Because no single mechanism was responsible for densification in any one region, the calculated Q's are apparent activation energies. These values are tabulated in table 3.

Values ranging from 29–91 kJ/mol were calculated for region C. These values are in close agreement with those previously reported in other gel systems. Prassas (ref. 5 calculated activation energies from 21 to 42 kJ/mol for a silica aerogel in the temperature range 500–850°C. These values are of the same order of magnitude as those for the condensation reaction

$$2H_4SiO_4 \longrightarrow H_6Si_2O_7 + H_2O \qquad (6)$$

The activation energies listed in table 3 for viscous flow are low, but not unusually so, for gel-derived materials. For silica aerogels Prassas calculated a value of 368 kJ/mol from CHR dilatometry. Brinker *et al.* (ref. 16) reported activation energies ranging from 125 to 510 kJ/mol for viscous flow of an acid-catalyzed borosilicate gel. This wide range was found to be linearly related to the hydroxyl content of the gel. Differing values of activation energies are reported for the viscous flow of fused silica due to this residual hydroxyl content. Prassas (ref. 15) reported values between 502 to 711 kJ/mol corresponding to hydroxyl concentrations of 1300 to 3 ppm, respectively. Orgaz-Orgaz (ref. 5) reported 710 kJ/mol, comparable to the value accepted for pure fused silica, for base-catalyzed silica gels. Activation energies for viscous flow are also dependent on composition. Orgaz-Orgaz also reported activation energies of viscous flow for sintered colloidal gel-derived glasses of 598 kJ/mol for pure SiO_2 and 460 kJ/mol for silica with 3 wt% B_2O_3 added. Apparent activation energies for region E are midway between those of regions C and D. No significant difference could be assigned to the activation energies of this region. It is noteworthy that II.ABS.1 consistently exhibited virtually no shrinkage except at 1184°C in region E and hence its value of apparent activation energy is not included in table 3 for this region. In contrast to this densification behavior is II.ABS.2, which exhibited nearly four times the amount of shrinkage as I.ABS.1 after 1 h at 1146°C as shown in Figures 6 and 16. The activation energies

calculated in this range are considerably less than the 593–627 kJ/mol reported for solid state diffusion sintering (ref. 15). Therefore the densification in region E must result from several competing mechanisms.

Evaluation of Regions B and C

The mean coefficients of shrinkage reported for region C in table 1 show that a common mechanism exists for all methods with an overall mean value of $n = 0.74$. The mechanism(s) operative in region B apparently were still operative in region C as the difference in the means of the two regions is insignificant. From observations made in region B, it is apparent that capillary contraction contributed to shrinkage in this region. However, this mechanism would have been active during pre-calcination of the powders and should have been exhausted at this point. Observed weight loss data in region B for the ABS powder compacts (fig. 8) show a rapid decrease between 25 and 300°C. This weight loss is concurrent with a slight increase in apparent density and a slight decrease in bulk density (fig. 14). IR spectra show a decreasing absorption due to water and hydroxyl ions as they are being slowly evolved in this temperature range (fig. 11). These observations could be due to atmospheric moisture being physically adsorbed onto the highly reactive surface of the powders after pre-calcination. The vaporization of this water accounts for the initial high weight loss observed in figure 8. The diffusion of water from the powder compact was responsible for the higher rates of densification at the lower temperatures of region B. As this water is gradually depleted, the dominant densification mechanism changes to condensation reactions already in progress. This also explains why no initial decrease in apparent density was observed in the temperature range corresponding to the decrease in bulk density. The skeletal structure had already been developed for the most part during the pre-calcination stage of processing as was evidenced by the 28% increase in apparent density (ref. 4). Therefore, additional firing of the powder compacts at the temperatures of region B had little effect on apparent density. The changes in apparent density do not come about until sufficient energy is available to drive additional condensation reactions. The required energies are listed in table 3.

The shrinkage coefficient of region C is too large for the densification mechanism to be due to condensation reactions alone. It is well established that condensation reactions are diffusion controlled where $n = 0.5$ (ref. 7). Therefore, densification in this region is due to at least one other mechanism acting in concert with condensation. The continued weight loss throughout this region (fig. 8) is due to the elimination of condensation reaction by-products. Another possible contributing mechanism is structural relaxation. Structural relaxation is achieved by the diffusive motions of atoms without the expulsion of water or other species. It occurs as the gel structure seeks a configuration more characteristic of the corresponding metastable liquid. Brinker *et al.* (ref. 16) reported structural relaxation in a borosilicate gel in the temperature interval 400°C–525°C. If the gels have different structures at the onset, then the contribution of structural relaxation will differ, the shrinkage coefficients will differ, and the activation energies will differ. A mechanism which assists the structure in seeking a more stable state will increase the rate of densification and therefore increase the shrinkage coefficient and decrease the activation energy, as was observed in region C. Structural relaxation would further densify the skeletal structure resulting in an increase in apparent density as observed in figure 14. The slight decrease in bulk density in regions B and C show that the weight loss was slightly greater than the volume contraction.

Evalution of Region D

Viscous flow in the ABS powders occurred in the narrow temperature range of 800°C to the crystalline transformation temperature (T_t). It is obvious from figure 5 that shrinkage in this region was very sensitive to temperature as is the case for vitrification processes. Generally, greater shrinkage occurred at temperatures near T_g than near T_t. This is particularly evident in the 875°C experiment (fig. 5(a)). Only 2% shrinkage was observed at this temperature and all of this shrinkage occurred within the first five minutes of the run.

Figure 14 shows that a rapid increase in bulk density occurred from 690 to 845°C while the apparent density increased more gradually. Little weight loss was recorded in this temperature range (fig. 8). The inflection of the lower curve of figure 14 was due to a sharp decrease in the bulk volume with little loss in weight. Compared to region C, the weight loss in region D was minimal so condensation reactions apparently did not contribute substantially to this shrinkage. A rapid reduction in the bulk volume due to the collapse of open

pores could account for the observed changes in properties. These observations are characteristic of viscous flow.

The deviation of region D shrinkage data from ideal viscous sintering, as modeled by Frenkel, appeared to result from increasing viscosity. Similar behavior in the viscous sintering of alkoxide-derived gels has been reported (refs. 7 and 16). The viscosity of glass is dependent on the hydroxyl content and temperature. The viscosity decreases with increasing OH^- concentration. Retained water and hydroxyls in the ABS gels up to 690°C was evident from the IR spectra of figure 11(a) and (b). It has been shown that increasing the water content depresses T_g (ref. 17). Figure 3 of reference 4 shows a change in slope from DTA for all methods at about 835°C which was indirectly attributed to T_g. Because similar behavior was oberved in the DTA, it was assumed that the OH^- concentration was equal for all powders. Hence the water and hydroxyls retained upon entry into region D provided a viscosity sufficient for ideal viscous sintering. As sintering proceeded, the OH^- concentration decreased, increasing the viscosity and dampening the shrinkage rate.

Brinker *et al.* (ref. 16) pointed out that structural relaxation as well as the condensation of hydroxyls can occur during viscous sintering and have an important influence on the rate of shrinkage. His estimates for a borosilicate alkoxide gel at 525°C suggests that structural relaxation may cause a significant fraction of the viscosity increase, but that changing hydroxyl ion content is probably the dominant factor. Relaxation will cause smaller changes in shrinkage during isothermal conditioning (soak) at higher temperatures as relaxation will occur during heating to the soak temperature. However, hydroxyl loss will be less at higher temperatures as they are continuously evolved during the ramp to the isothermal hold temperature. Because structural relaxation and condensation mechanisms were active in region C prior to the onset of viscous flow, it was concluded that both mechanisms were active in region D. The data accumulated from this region suggest that residual OH^- was more influential than structural relaxation. Because there were fewer hydroxyls at the higher temperatures of this region, the viscosity increased more rapidly. This resulted in less shrinkage than that observed at lower temperatures. The IR spectrum for ASB based powders shows that this process trapped some water and hydroxyls within their structure. This suggests that the ASB based compacts were initially more dense than the AIP and could account for the factor-of-four difference in the extent of shrinkage due to viscous flow. The morphologies of the ASB and AIP base agglomerates (fig. 4, ref. 4) also supports this observation.

There is one other pertinent feature in region D from the IR spectra. This is the gradual elimination of the absorption band at 1415 cm^{-1} "c" assigned to B-O-Si. This adsorption rapidly decreases in the short temperature interval of 845°–864°C. This is indicative of bond cleavage in the B-O-Si network during viscous sintering and the dissolution of Si^{+4} and B^{+3} into a phase-separated glass. The result appears to be the formation of a boria-rich and silica-rich glass that would surround the aluminum borate and mullite crystalline phases.

Evaluation of Region E

The overall mean value of n for region E is 0.73, nearly equal to that of region C. The apparent activation energy, however, is considerably higher. The transition from region D to region E was marked by an abrupt decrease in shrinkage as indicated in figure 2. XRD showed that an ordered phase crystallized at the temperatures corresponding to this transition. Analysis of CHR data revealed the temperature of this transformation within ±2°C. It was found that for Method I powders T_t = 888°C while for Method II powders T_t = 895°C.

A comparison of figures 6 and 16 shows that the shrinkage in compacts made from ASB was considerably greater than those from AIP. The shrinkage incurred in this region however, was the least of all regions examined. Powder compacts with AIP as an aluminum precursor exhibited no measurable shrinkage at 950°C whereas those from ASB did. Oddly enough, the greatest shrinkage for all compacts occurred at 1146°C rather than the higher temperature of 1184°C. This is reflective of earlier densification behavior, specifically that in region C.

The differences among the synthesis methods in this region seem to be due to the remnants of structural differences from earlier densification. It is thought that the various structures incorporated the boria precursor in the polymeric network at different rates which in turn determined the type and extent of oxygen-boron-oxygen-metal linkages formed. At high temperatures this affected the amount of boria that entered into

the phase-separated glass and crystalline phases. The powder compacts relatively abundant (ref. 2) in boron-rich glass underwent more densification in region E due to viscous sintering than those with less. Also the vapor pressure of boria over a boron-rich glass phase would be higher than that in a silica-rich glass phase. This may explain the increase in weight loss observed at the higher temperatures of this region as shown in figure 2 (ref. 4) and figure 8. Figure 4 (ref. 4) shows that ASB based powder compacts contained more of a glassy phase than did the AIP based material and because of the effects just described could account for the observed behavior in this region.

The micrographs of figures 12 and 13 as well as the results of the previously mentioned crystallite size analysis showed that grain growth occurred in this region as well. The values of Q are too small to be due to grain growth alone and the shrinkage coefficients are too large to be due to solid state diffusion ($0.3 < n < 0.5$) (refs. 5 and 18). Therefore, densification in region E is due to a competition between grain growth and boria assisted viscous sintering.

Summary

Aluminoborosilicate powders with the molar ratio 3:1:2 ($Al_2O_3 \cdot B_2O_3 \cdot SiO_2$) were prepared by the sol-gel route. Structural irregularities incorporated into the gels by these methods resulted in diverse densification behavior at low, intermediate, and high temperatures.

Five regions of densification were observed in the temperature range 25–1184°C for all powders. The regions were labeled A–E from low to high temperature. Region A (25–100°C) was probably due to capillary contraction. This was not observed directly because it occurred during the pre-calcination stage of processing. Hence, the observed region A was inert having no shrinkage and no measurable weight loss. Region B (100–400°C) was due to the elimination of adsorbed water and condensation reactions. Region C (400–800°C) resulted from condensation reactions and structural relaxation. Densification in region D (800–T_t) was from viscous sintering. Shrinkage in this region decreased with increasing viscosity. The increase in viscosity was attributed primarily to a decrease in the [OH^-] during sintering. Generally, greater shrinkage was observed at temperatures nearer to T_g than those near T_t. B-O-Si bond disruption occurred in this region and indicated the formation of a phase-separated glass. region E (T_t–1184°C) was caused by several competing mechanisms. Grain growth and boria fluxed viscous flow were probably the dominant mechanisms here.

All powders crystallized a multiphasic structure consisting of a phase separated glass and nonequilibrium forms of mullite, aluminum oxide borate and aluminum borate at T_t. ABS powder compacts increased in bulk density by 80% and in apparent density by 32%. Hardness measurements paralleled trends in bulk density with the greatest hardness appearing in region D.

The behavior shown here is reflective of the different polymeric networks established during synthesis and their domination of physical processes at elevated temperatures. It appears that the ABS powders retained these structural variations at temperatures approaching the fusion point ($\approx 0.85\ T_m$ for II.ABS.2). Such information could be used in designing ABS materials with tailored thermochemical properties otherwise unattainable in conventional powders for high-temperature applications.

References

1. Brinker, C. J.; and Mukherjee, S. P.: Conversion of Monolithic Gels to Glasses in a Multicomponent Silicate Glass System, J. Mater. Science, vol. 16, 1981, pp. 1980-88.

2. Yoldas, B. E.: Preparation of Glasses and Ceramics from Metal-Organic Compounds, J. Mater. Sci., vol. 12, 1977, pp. 1203-8.

3. Yoldas, B. E.: Effect of Variations in Polymerized Oxides on Sintering and Crystalline Transformations, J. Am. Ceram. Soc., vol. 65, no. 8, 1982, pp. 387-93.

4. Bull, J. D.; Selvaduray, G.; and Leiser [illegible] B.: Sol-Gel Synthesis and Densification o[illegible]i-noborosilicate Powders; Part I; TM-103964, 1992.

5. Prassas, M.; Phalippou, J.; and Zarzychi, J.: Sintering of Monolithic Silica Aerogels; Chapter 17, pp. 156-57 in Science of Ceramic Chemical Processing. Edited by L. L. Hench and D. R. Ulrich, John Wiley and Sons, Inc., New York, NY, 1986.

6. Lay, K. W; and Carter, R. E.: Time and Length Corrections in the Analysis of the Initial Stages of Diffusion, J. Am. Ceram. Soc., vol. 52, no. 4, 1969, pp. 189-91.

7. Orgaz-Orgaz, F.: Gel to Glass Conversion: Densification Kinetics and Controlling Mechanisms, J. Non-Cryst. Solids, vol. 100, 1988, pp. 115-41.

8. JCPDS, Card Nos. 15-776, 34-1039, and 32-3. International Centre for Diffraction Data, Swathmore, PA, 1989.

9. Cullity, B. D.: Elements in X-Ray Diffraction, 2nd edition, pp. 284-85. Addison-Wesley Publishing Co., Reading, MA, 1978.

10. Scherer, G. W.: Sintering of Low-Density Glasses: I, Theory, J. Am. Ceram. Soc., vol. 60, nos. 5-6, 1977, pp. 236-39.

11. Xiaoming, L.; and Yuguang, W.: Some Characteristics of Glass in the Al_2O_3-B_2O_3-SiO_2 System from the Gel, J. Non-Cryst. Solids, vol. 80, 1986, pp. 564-70.

12. Risbud, S. H.; and Zangvil, A.: Microchemistry and Microstructure of a Multiphase Aluminosilicate Ceramic, J. Mater. Sci., vol. 18, 1983, pp. 998-1004.

13. Charles, R. J.; and Wagstaff, F. E.: Metastable Immiscibility in the B_2O_3·SiO_2 System, J. Am. Ceram. Soc., vol. 51, no. 1, 1968, pp. 16-20.

14. Brinker, C. J.; Roth, E. P.; Scherer, G. W.; and Tallant, D. R.: Structural Evolution During the Gel to Glass Conversion, J. Non-Cryst. Solids, vol. 71, 1985, pp. 171-85.

15. Sintering of Glass Powders During Constant Rates of Heating, J. Am. Ceram. Soc., vol. 52, no. 1, 1969, pp. 14-17.

16. Brinker, C. J.; Scherer, G. W.; and Roth, E. P.: Sol→Gel →Glass: II. Physical and Structural Evolution During Constant Heating Rate Experiments, J. Non-Cryst. Solids, vol. 72, 1985, pp. 345-68.

17. Tanka, H.; Yazawa, T.; and Eguchi, K.: Sintering Temperature of Porous Glass and Transition Temperature of High Silica Glass, Yogyo-Kyokai-Shi, vol. 94, no. 6, 1986, pp. 564-70.

18. Kingery, W. D.; Bowen, H. K.; and Uhlmann, D. R.: Introduction to Ceramics, 2nd edition, p. 448. John Wiley and Sons, Inc., New York, NY, 1976.

Table 1. Mean coefficients of shrinkage for regions B, C, and E from isothermal TDA of ABS powder compacts

Method	Shrinkage coefficient, n		
	Region B	Region C	Region E
I.ABS.1		0.65	0.81
I.ABS.2		0.77	0.67
II.ABS.1		0.87	
II.ABS.2	0.70	0.68	0.72

Table 2. Crystallite size variation with temperature in synthesized ABS powders

Temperature, °C	Crystallite size, Å			
	I.ABS.1	I.ABS.2	II.ABS.1	II.ABS.2
864	90	99	99	
1049	110	108	119	108
1184	137	150	129	145

Table 3. Apparent activation energies for major regions of shrinkage in synthesized ABS powders

Method	Activation energy, kJ/mol		
	Region C	Region D	Region E
I.ABS.1	29	489	232
I.ABS.2	55	414	254
II.ABS.1	91	410	
II.ABS.2	54	448	298

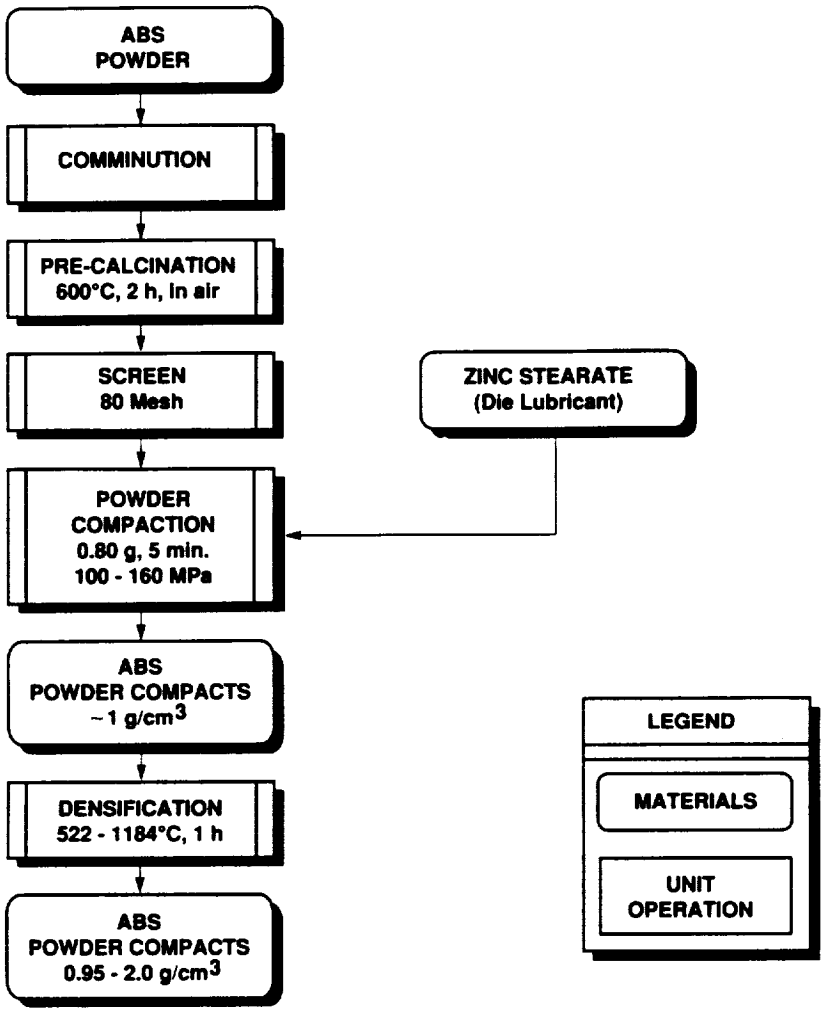

Figure 1. Flow diagram of post synthesis processing of ABS powders.

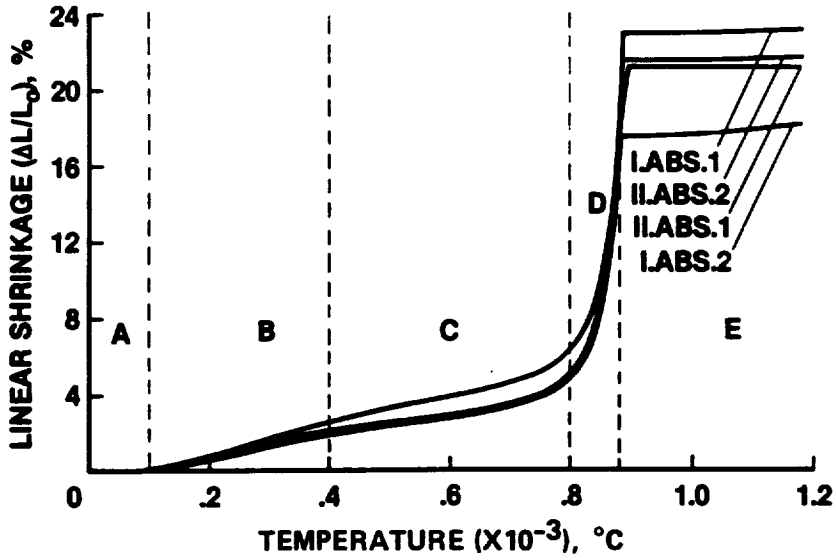

Figure 2. Linear shrinkage of ABS powder compacts showing five regions of shrinkage.

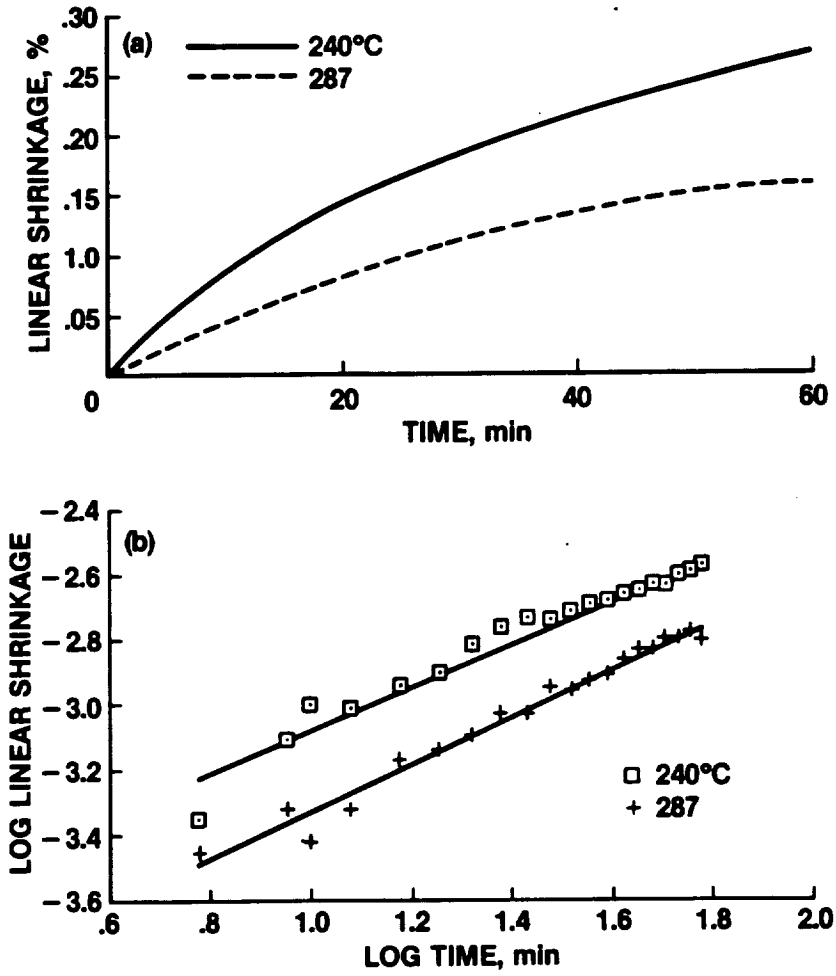

Figure 3. Isothermal shrinkage plots for II.ABS.2 region B; (a) linear shrinkage vs. time, (b) log linear shrinkage vs. log time.

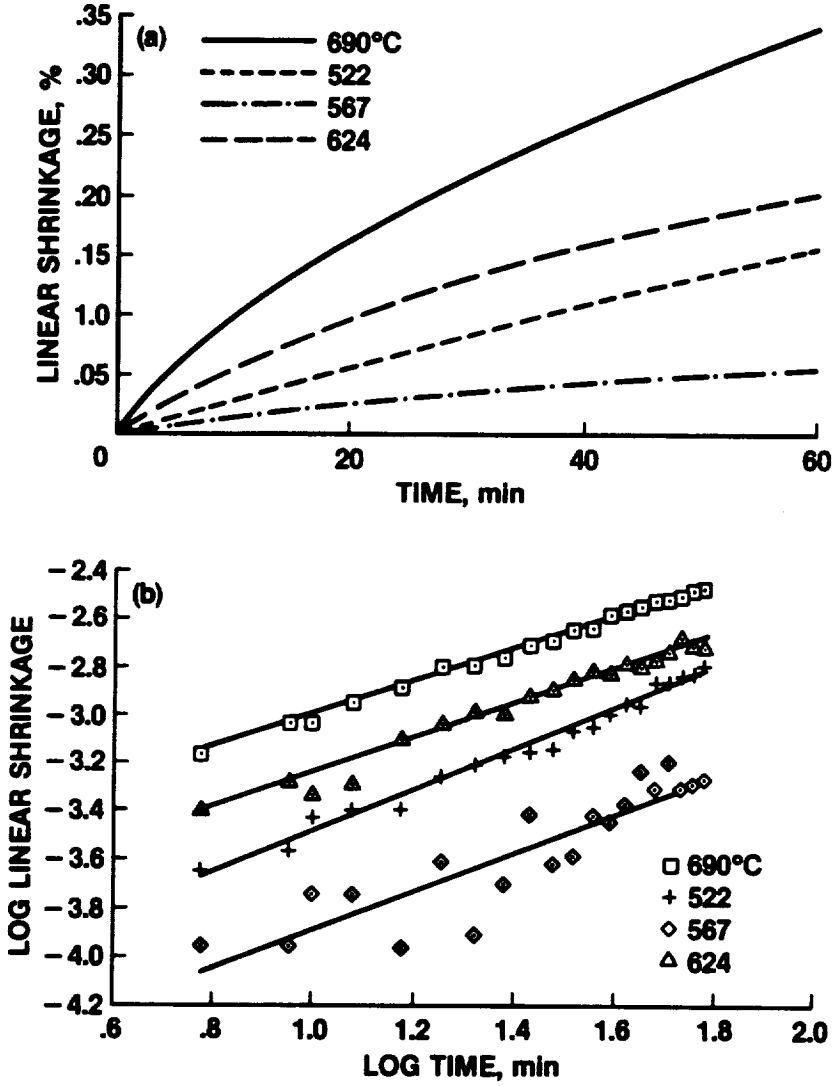

Figure 4. Isothermal shrinkage plots for I.ABS.2 region C; (a) linear shrinkage vs. time, (b) log linear shrinkage vs. log time.

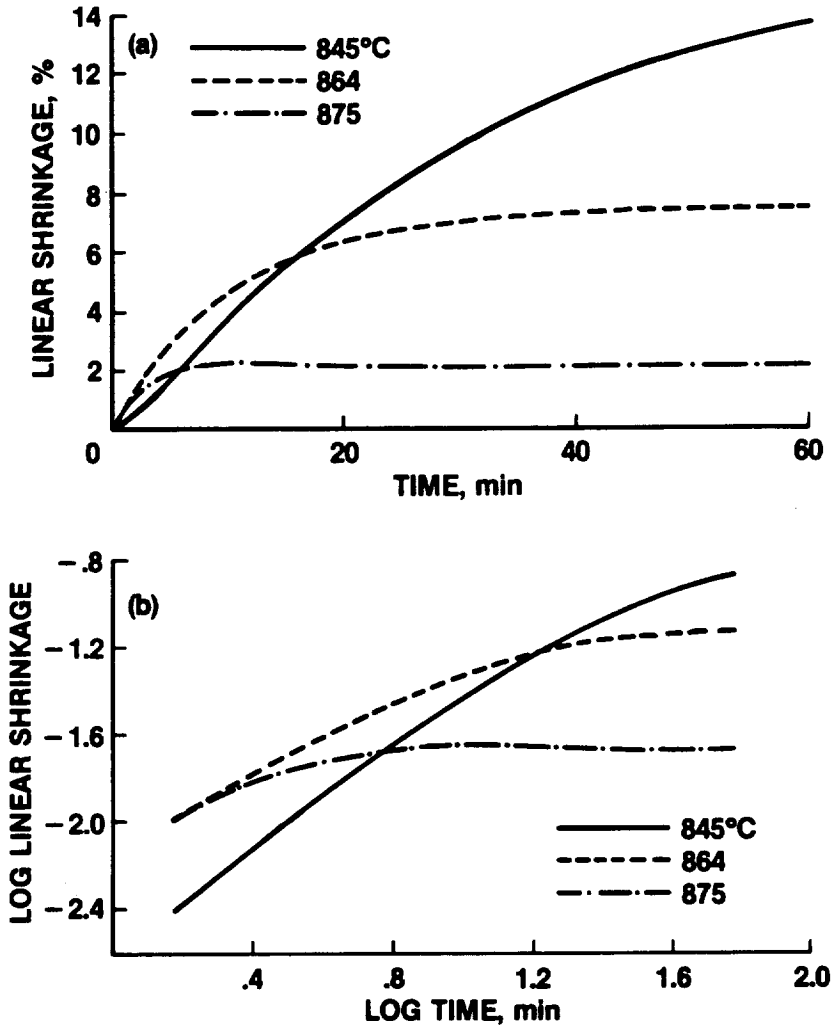

Figure 5. Isothermal shrinkage plots for I.ABS.1 region D; (a) linear shrinkage vs. time, (b) log linear shrinkage vs. log time.

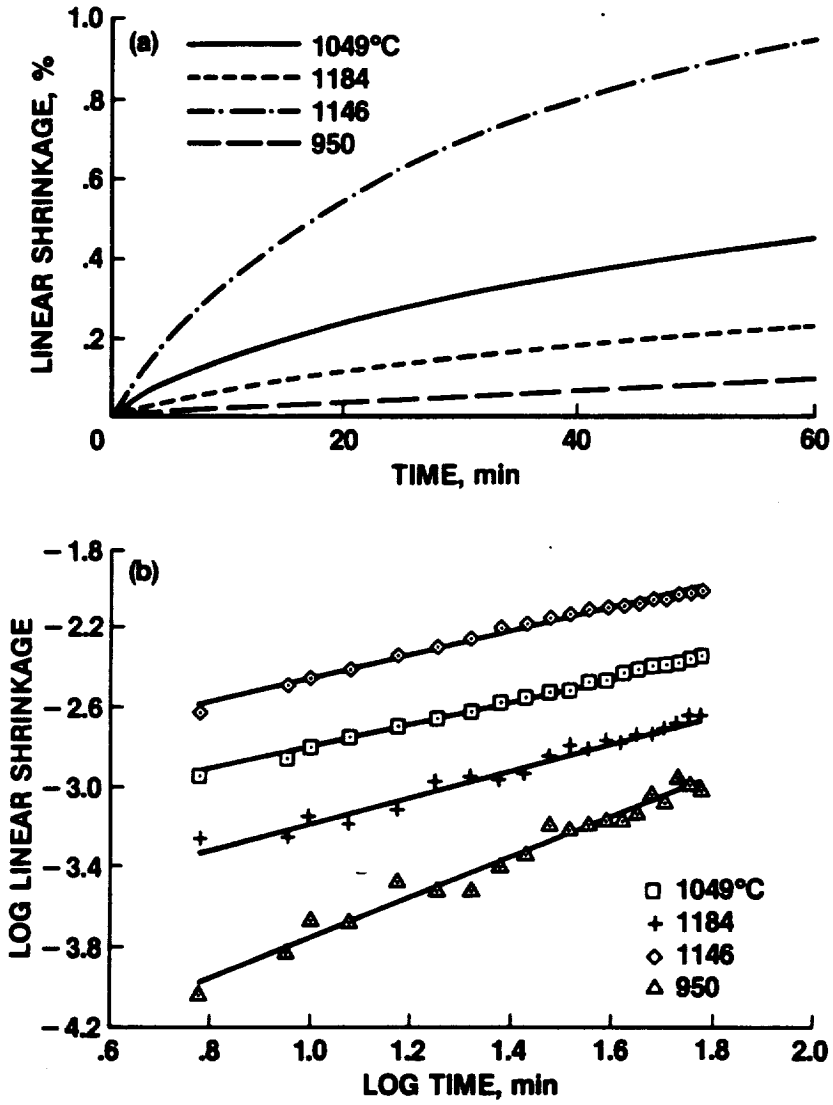

Figure 6. Isothermal shrinkage plots for I.ABS.1 region E; (a) linear shrinkage vs. time, (b) log linear shrinkage vs. log time.

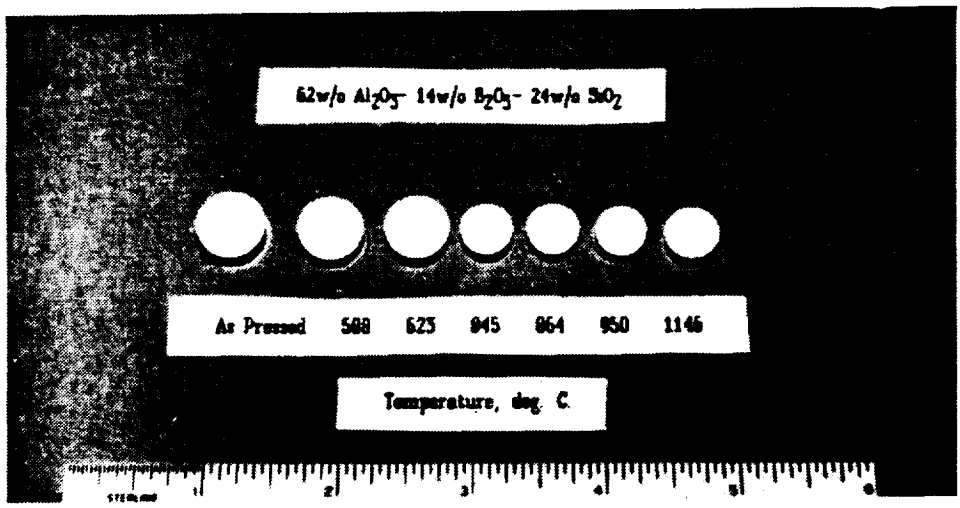

Figure 7. Variation in shrinkage of ABS powder compacts after exposure to the indicated temperature for 1 h.

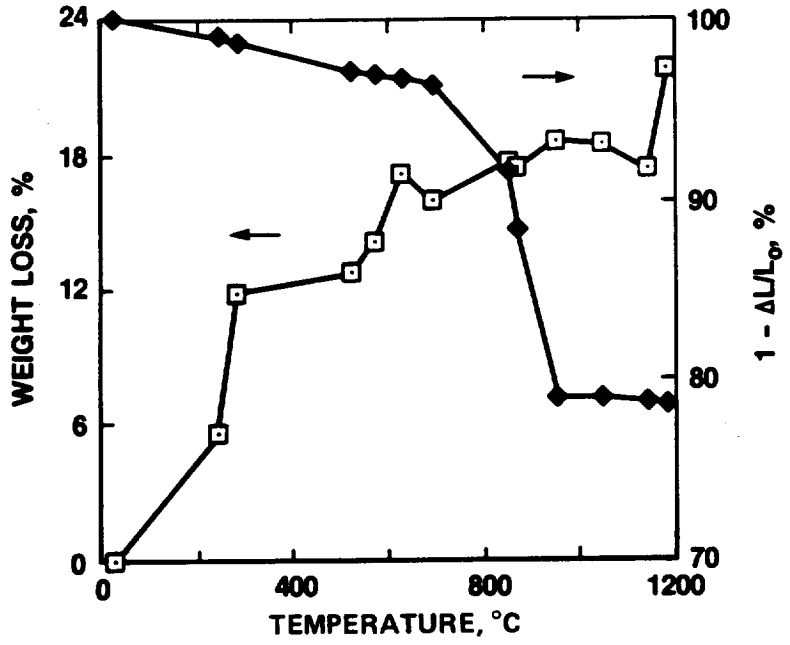

Figure 8. Mean recorded weight loss and fractional shrinkage of ABS powder compacts after 1 h at temperature.

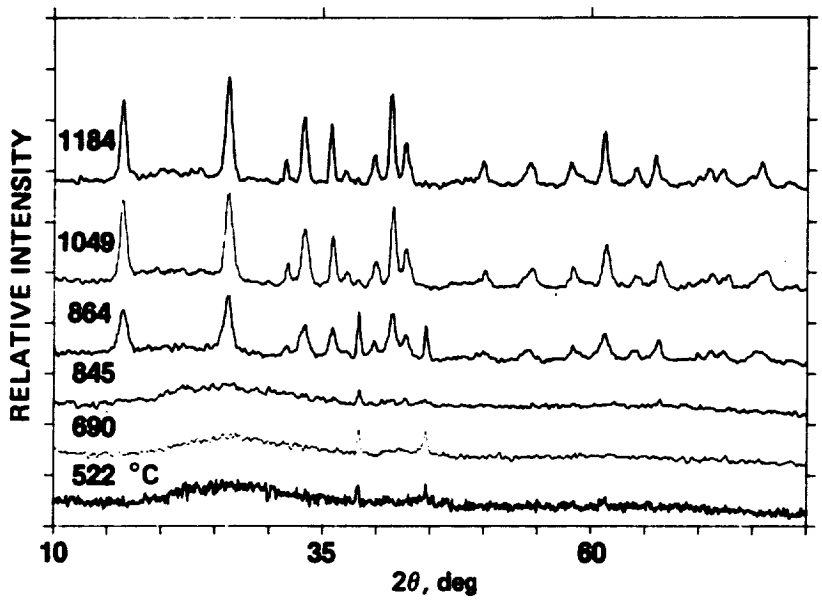

Figure 9. X-Ray diffraction patterns of II.ABS.2 after 1 h at temperature. Numbers in pattern indicate temperature in °C.

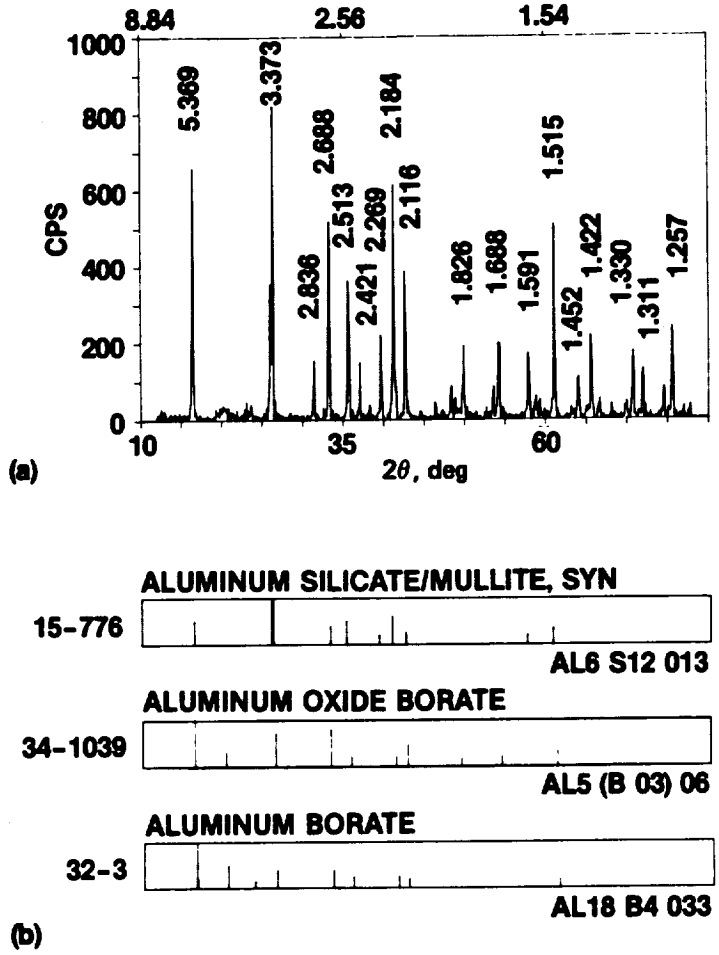

Figure 10. (a) X-Ray diffraction pattern of II.ABS.2 after 1 h at 1400°C showing intensity and d-spacing of diffraction lines, (b) Same as (a) but showing normalized intensity and stick pattern of three phases identified in the ABS powders.

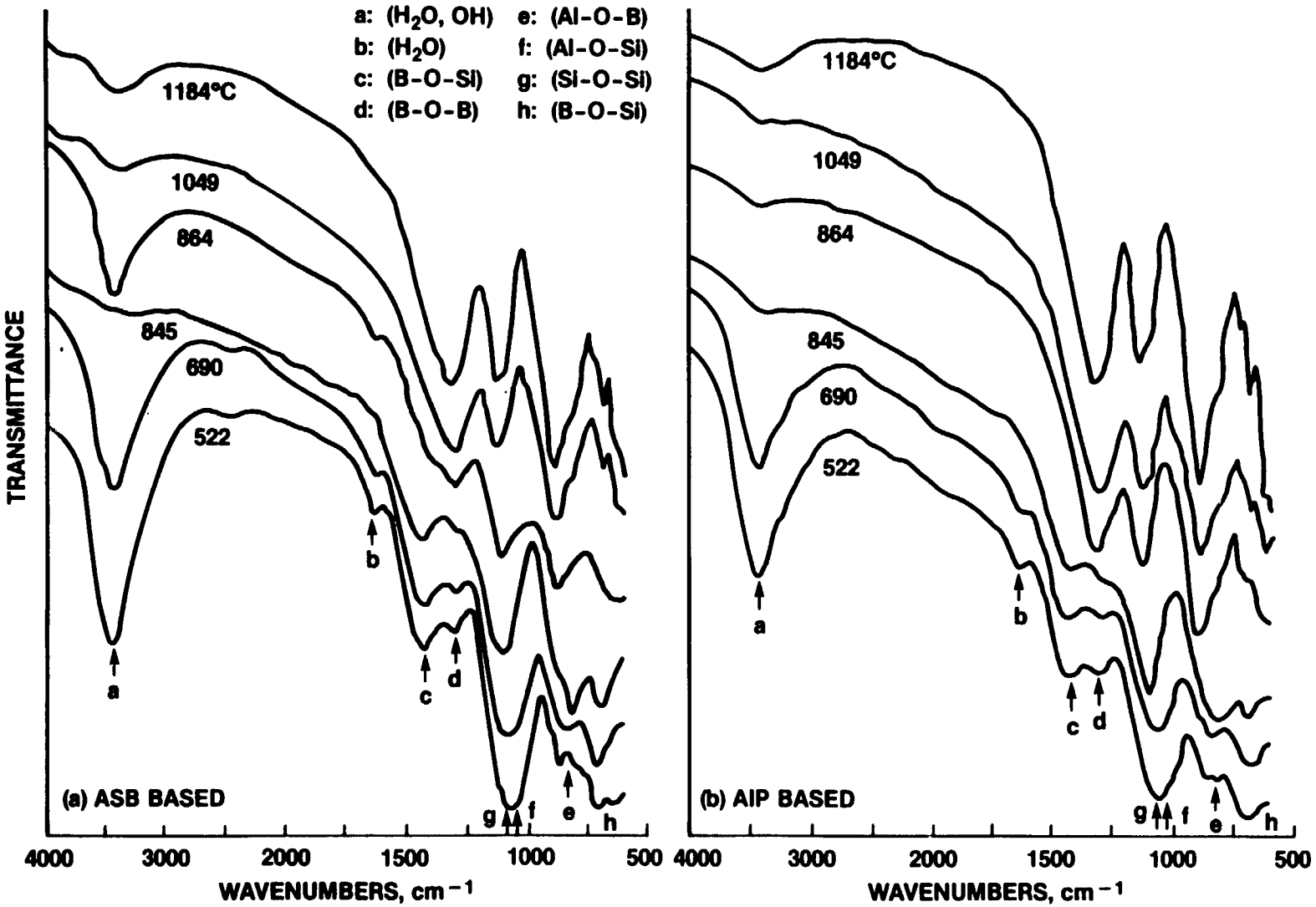

Figure 11. Infrared spectra of synthesized ABS powders after firing for 1 h at the indicated temperature; (a) ASB based powder, (b) AIP based powder.

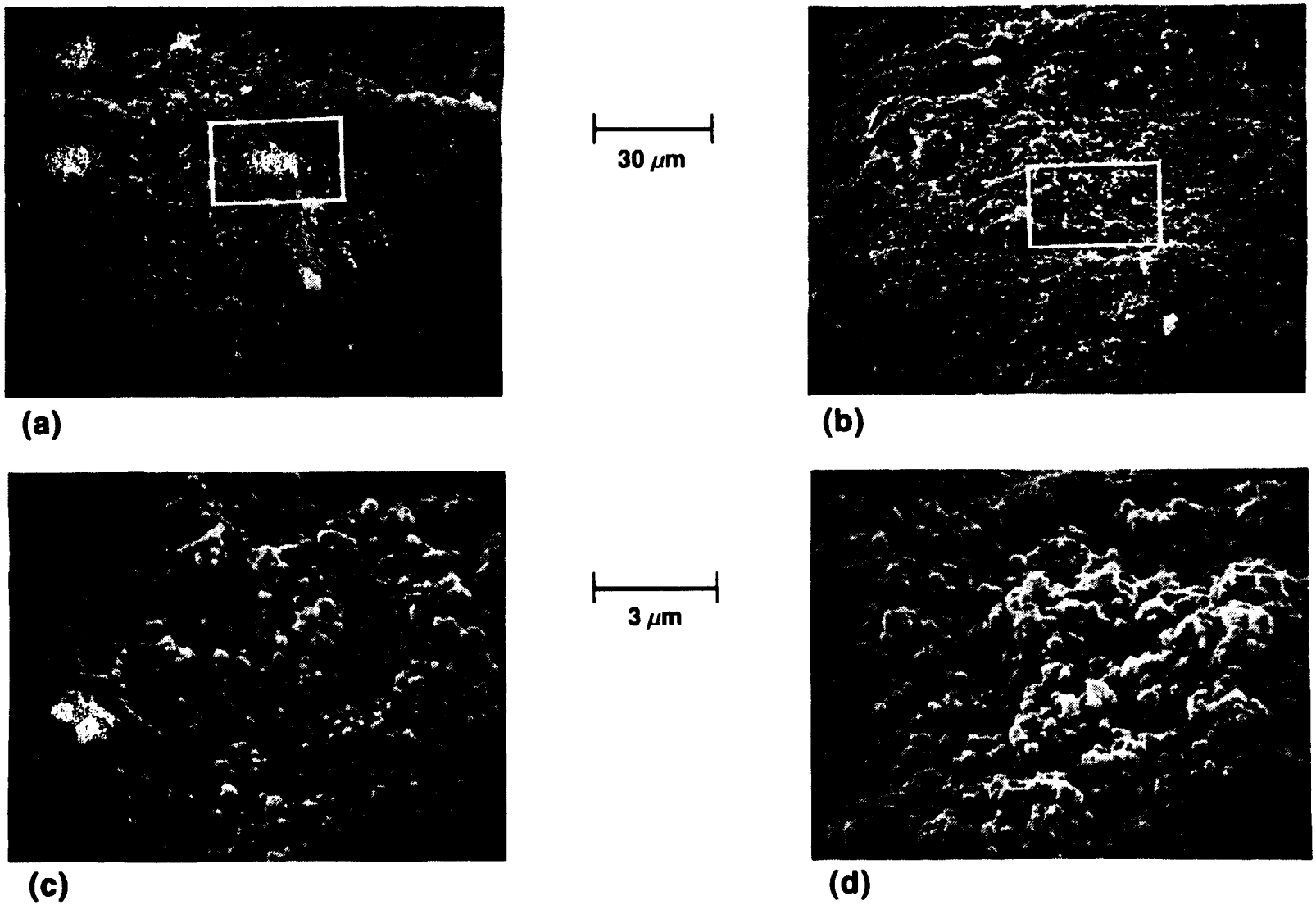

Figure 12. SEM micrographs of fractured surface of AlP based powder compacts; (a) as pressed; (b) after 1 h at 1184°C, (c) 10X magnification of boxed area in (a), (d) 10X magnification of boxed area in (b).

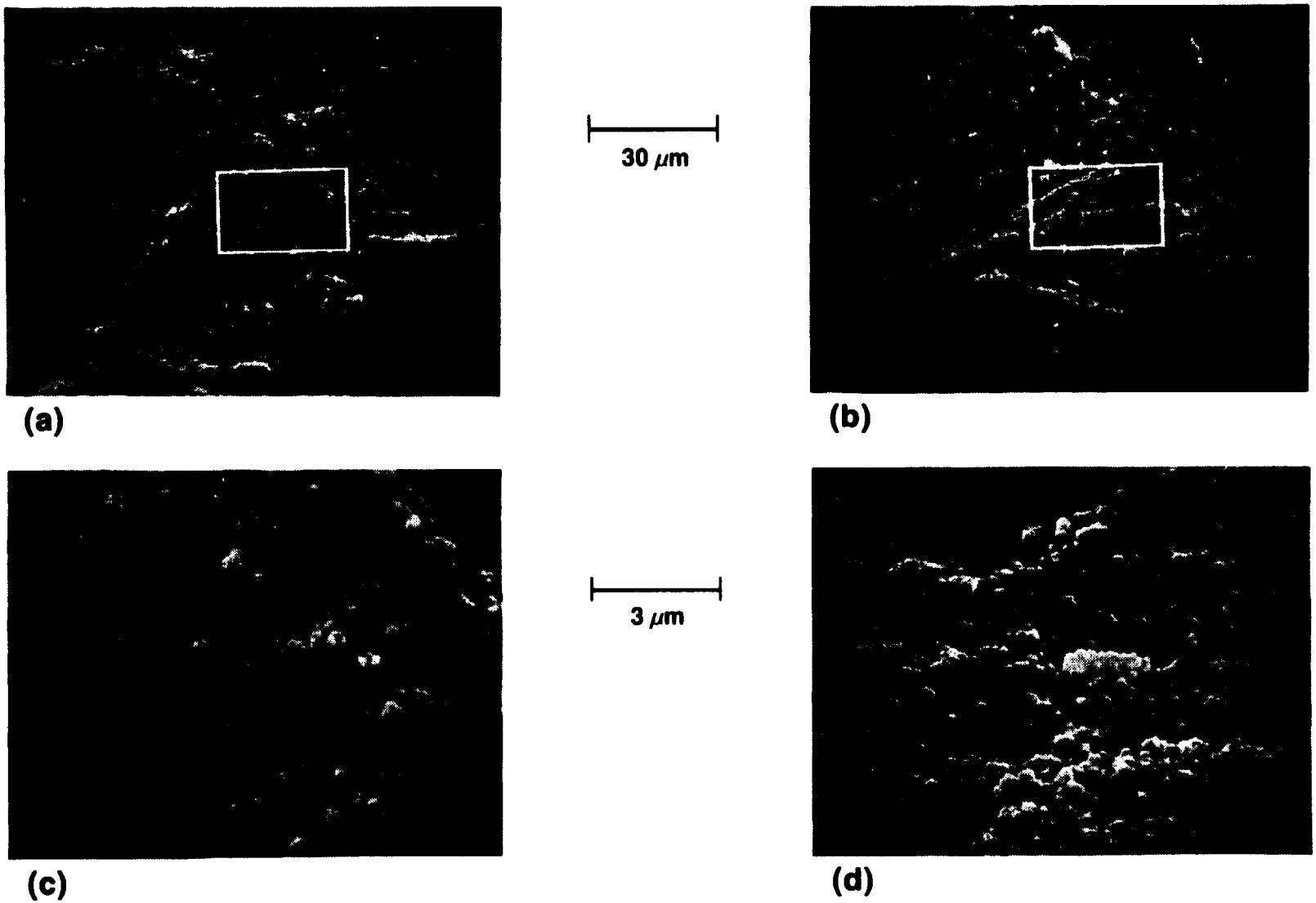

Figure 13. SEM micrographs of fractured surface of ASB based powder compacts; (a) as pressed; (b) after 1 h at 1184°C, (c) 10X magnification of boxed area in (a), (d) 10X magnification of boxed area in (b).

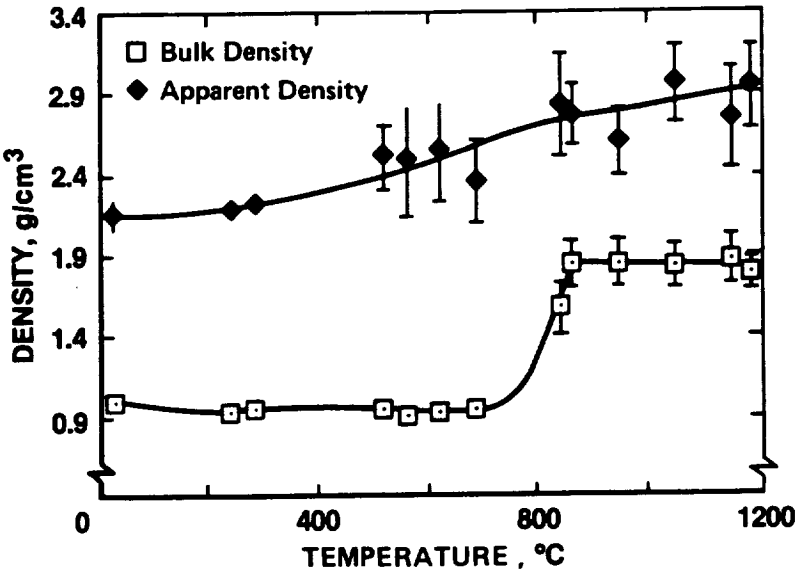

Figure 14. Mean bulk and apparent density of ABS powder compacts as a function of temperature. Measurements made after 1 h at temperature.

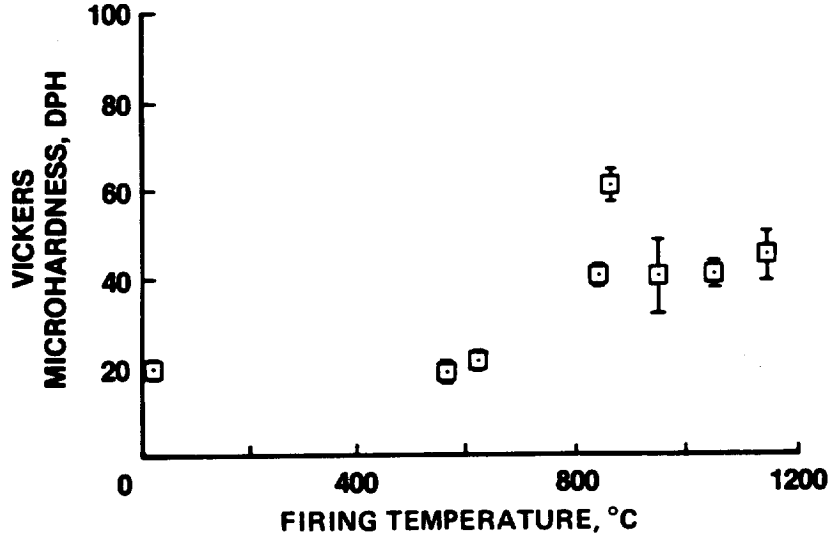

Figure 15. Vickers microhardness of II.ABS.1 powder compacts after heat treatment.

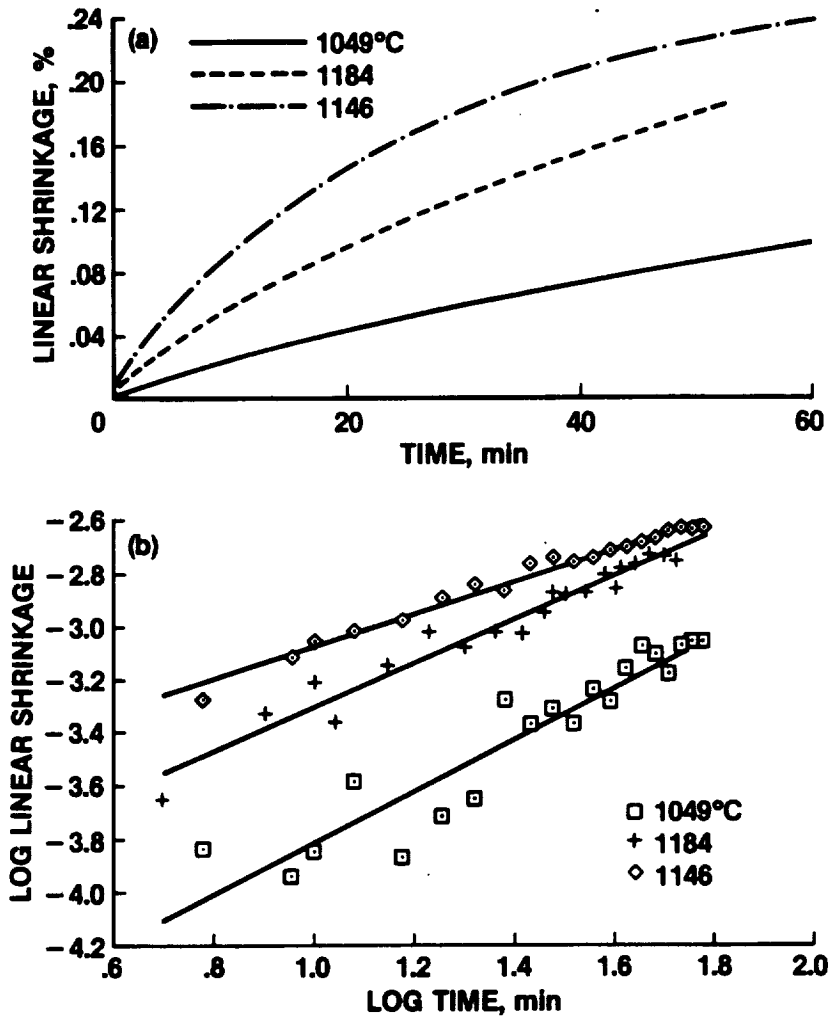

Figure 16. Isothermal shrinkage plots for II.ABS.2 region E; (a) linear shrinkage vs. time, (b) log linear shrinkage vs. log time.

REPORT DOCUMENTATION PAGE

Form Approved
OMB No. 0704-0188

1. AGENCY USE ONLY *(Leave blank)*	2. REPORT DATE	3. REPORT TYPE AND DATES COVERED
	September 1992	Technical Memorandum

4. TITLE AND SUBTITLE

Sol-Gel Synthesis and Densification of Aluminoborosilicate Powders
Part 2–Densification

5. FUNDING NUMBERS

506-43-31

6. AUTHOR(S)

Jeffrey Bull, Guna Selvaduray (San Jose State University, San Jose, CA), and Daniel Leiser

7. PERFORMING ORGANIZATION NAME(S) AND ADDRESS(ES)

Ames Research Center
Moffett Field, CA 94035-1000

8. PERFORMING ORGANIZATION REPORT NUMBER

A-92174

9. SPONSORING/MONITORING AGENCY NAME(S) AND ADDRESS(ES)

National Aeronautics and Space Administration
Washington, DC 20546-0001

10. SPONSORING/MONITORING AGENCY REPORT NUMBER

NASA TM-103969

11. SUPPLEMENTARY NOTES

Point of Contact: Jeffrey Bull, Ames Research Center, MS 234-1, Moffett Field, CA 94035-1000
(415) 604-5377

12a. DISTRIBUTION/AVAILABILITY STATEMENT

Unclassified-Unlimited
Subject Category – 23

12b. DISTRIBUTION CODE

13. ABSTRACT ***(Maximum 200 words)***

Aluminoborosilicate (ABS) powders, high in alumina content, were synthesized by the sol-gel process utilizing four different methods of synthesis. The effect of these methods on the densification behavior of ABS powder compacts was studied. Five regions of shrinkage in the temperature range 25–1184°C were identified. In these regions, the greatest shrinkage occurred between the gel-to-glass transition temperature ($T_g \sim 835°C$) and the crystallization transformation temperature ($T_t \sim 900°C$). The dominant mechanism of densification in this range was found to be viscous sintering. ABS powders were amorphous to X-rays up to T_t at which a multiphasic structure crystallized. No $2Al_2O_3 \cdot B_2O_3$ was found in these powders as predicted in the phase diagram. Above T_t densification was the result of competing mechanisms including grain growth and boria fluxed viscous sintering. Apparent activation energies for densification in each region varied according to the method of synthesis.

14. SUBJECT TERMS

Aluminoborosilicate, Sintering, Densification, Powder, Sol-gel, Glass

15. NUMBER OF PAGES

23

16. PRICE CODE

A02

17. SECURITY CLASSIFICATION OF REPORT	18. SECURITY CLASSIFICATION OF THIS PAGE	19. SECURITY CLASSIFICATION OF ABSTRACT	20. LIMITATION OF ABSTRACT
Unclassified	Unclassified		